75th International Astronautical Congress (IAC), Milan, Italy, 14-18 October 2024.
Copyright ©2024 by the International Astronautical Federation (IAF). All rights reserved.

IAC-24,C2,8,11,x84083

Binder jetting of lunar regolith: 3d printing and densification

Marco Mariani[a], Francesco Bertolini[a], Maxim Isachenkov[b]*, Carmen Galassi[a], Nora Lecis[a], Antonio M. Grande[b], Giuseppe Sala[b]

[a] *Department of Mechanical Engineering, Politecnico di Milano, via La Masa 1, Milano 20156, Italy*
[b] *Department of Aerospace Science and Technology, Politecnico di Milano, via La Masa 34, Milano 20156, Italy*
* Corresponding Author: maxim.isachenkov@polimi.it

Abstract

The establishment of a human presence on the Moon necessitates the development of sustainable technologies for in-situ resource utilization, enabling the conversion of lunar resources into functional raw materials. Binder jetting is promising for employing regolith, the material found on the lunar surface, as a feedstock for additive manufacturing. This approach offers several advantages, such as the layer-by-layer creation of complex and customized structures catering to specific needs and functionalities, the potential for automation (minimizing the need for human intervention), and the simple processing of components without the need for high-energy sources as laser or electron beams. However, implementing binder jetting on the Moon presents unique challenges. The lunar regolith, with its extremely fine, jagged particles necessitates the optimization of the printing process and the understanding of densification mechanisms from a loosely packed green body to achieve the desired mechanical properties. In this study, an analysis of the printing parameters, such as layer thickness (50-100 µm), binder saturation (70-90%), and drying conditions, on the semi-finished and final components was performed to obtain a consistent and reliable fabrication of parts in terms of packing density and geometrical accuracy. The effect of feedstock granulometry and composition was considered to determine whether it affects the consolidation of parts. Regarding sintering, holding time and temperature were varied to assess the evolution of residual porosity and chemical composition according to the thermal treatment performed. Optical and scanning electron microscopies were employed to determine the distribution of voids, which were revealed to be correlated to the initial layerwise buildup of specimens. Energy dispersive x-ray spectroscopy combined with x-ray diffraction identified the formation and distribution of Al-, Si-, Fe-, and Ti-based oxides. Finally, preliminary mechanical testing was conducted to determine the strength of the densified components and anisotropic response owing to internal microstructural features.

Keywords: Binder Jetting; Lunar Regolith; In-situ Resource Utilization; Additive Manufacturing; 3D Printing; Sintering.

Acronyms/Abbreviations

AM	Additive Manufacturing
BJT	Binder Jetting
BST	Binder Set Time
CCC	Cement Contour Crafting
DLP	Digital Light Processing
DT	Drying Time
EDX	Energy Dispersive X-ray
HV	Vickers Hardness
ISRU	In-situ Resource Utilization
PBF	Powder Bed Fusion
PEG	Polyethylene Glycol
ROLS	Roller Speed
ROLTS	Roller Traverse Speed
RS	Recoat Speed
SEM	Scanning Electron Microscopy
SLA	Stereolithography
SLM	Selective Laser Melting
SMWS	Selective Microwave Sintering
SSLS	Selective Solar Light Sintering
TBT	Target Bed Temperature
UI	Ultrasonic Intensity
XRD	X-Ray Diffraction

1. Introduction

The renewed interest in lunar exploration has brought attention to the need for sustainable technologies that can support long-term human presence on the Moon. A key part of this vision is the idea of in-situ resource utilization (ISRU) [1], which involves using the lunar resources to produce essential materials and infrastructure, rather than totally relying on expensive and complicated supply missions from Earth. One of the most promising resources is lunar regolith, the loose, rocky material that covers the Moon's surface. Regolith could be used to make tools, parts, and even habitats through advanced manufacturing techniques, including additive manufacturing (AM) [2].

Several AM techniques have been preliminarily studied for use with lunar regolith [3]. The most extensively explored methods include Selective Laser Melting (SLM) / Powder Bed Fusion (PBF) [4], Selective Solar Light and Microwave Sintering (SSLS/SMWS) [5,6], Concrete-Like Construction Techniques (CCC - Cement Contour Crafting) [7], Stereolithography-based methods (including laser Stereolithography (SLA) and Digital Light Processing (DLP)) [8,9], and finally

Copyright ©2024 by the International Astronautical Federation (IAF). All rights reserved.

Material Extrusion/Ink-Jetting (MEX/IJT) [10] and Binder Jetting (BJT) [11].

SLM/PBF processes have been widely studied due to their ability to produce high-strength parts directly from regolith, without any additional binder. These methods allow to manufacture parts with complex geometries and produce components with significant mechanical strength; however, these methods require significant energy input, which can be a limitation in the lunar environment. SSLS and SMWS techniques also do not involve the use of binders and they are based on the exploitation of concentrated solar or microwave energy to sinter regolith directly. Solar sintering is especially appealing for the construction of large-scale lunar infrastructure (landing pads, pathways, blast walls, etc.) due to the abundant sunlight on the Moon's surface. Microwave sintering, on the other hand, leverages the Moon's lack of atmosphere to sinter regolith with the aid of intensive microwave radiation. The downside of these methods is the low printing resolution and low mechanical strength of produced parts, which significantly narrows down their applications.

All the other AM techniques, capable of using the lunar regolith as a feedstock, do require the use of a binder in the printing compositions. Among these methods, BJT stands out, as it offers distinct advantages such as lower energy requirements (compared to SLM/PBF) and the ability to automate the production process with minimal human oversight.

Despite its potential, the use of BJT with lunar regolith feedstock poses significant technical challenges. The unique properties of lunar regolith, including its heterogeneous mineral composition and presence of fine and irregularly shaped particles, demand a careful optimization of the printing and sintering processes to achieve mechanically robust and geometrically accurate ceramic components, especially in micro-gravity [12]. A critical aspect of this process is understanding the densification mechanisms that occur as the loosely packed green body sinters into a fully consolidated ceramic structure, especially if supersolidus liquid phase sintering occurs.

This study aims to address these challenges by systematically analyzing the key parameters involved in the BJT process when applied to lunar regolith. Parameters such as sintering temperature, heating rate, and dwell time are investigated, in relation to the resulting parts' density and shrinkage. Additionally, the study explores the impact of feedstock composition on the residual porosity and chemical composition of the manufactured ceramic parts. Through this research, we seek to contribute to the development of robust AM processes that can support sustainable lunar operations, paving the way for the establishment of a permanent human presence on the Moon.

2. Material and methods

2.1 Specimens manufacturing

The samples studied were manufactured with an LHS-1D simulant regolith powder, dust fraction of SRT's (former Exolith) Lunar Highland Regolith (LHS-1) [13]. The particle size distribution of LHS-1D was measured using a Malvern Mastersizer 2000 granulometer and it is presented in **Fig. 1**. The median particle size of LHS-1D was found to be 5.3 µm.

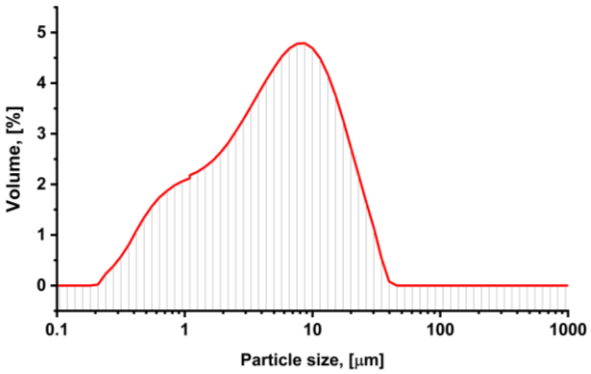

Fig. 1 Particle size distribution of LHS-1D

The powder was preheated at 80 °C to minimize the residual humidity to improve its flowability. BJT 3D printing was performed by an ExOne innovent+ machine. The layer thickness employed was 50 µm and the binder saturation (i.e. the ratio between the volume of binder deposited and the volume of pores in the powder bed) was set at 70% and 90% in different printing campaigns. The other parameters were kept constant, and they are listed in **Table 1**.

Table 1. Printing parameters employed in the BJT process (the acronyms are specified in the first paragraph).

TBT °C	BST sec	DT sec	RS mm s^{-1}	UI %	ROLS rpm	ROLTS mm s^{-1}
40	10	6	35	100	450	2

After printing, the powder bed was cured at 180 °C for 6 hours in air to promote the polymerization of polyethylene glycol (PEG), which allows to remove the green bodies from the excess powder by manual brushing. The parts were debinded and sintered in a single cycle: debinding was performed at 470 °C for 1 hour, whereas sintering conditions were varied as reported in **Table 2**, staying below the solidus temperature of the main phase according to previous studies [14]. To simulate the lunar atmospheric conditions, sintering was also carried out in low vacuum (10^{-2} mbar).

Copyright ©2024 by the International Astronautical Federation (IAF). All rights reserved.

Table 2. Temperature (T), dwelling times (t), heating rate (dT dt^{-1}), and atmosphere (Atm) of sintering treatments.

Sample	T °C	t h	dT dt^{-1} °C min^{-1}	Atm
1100_4_3	1100	4	3	Air
1150_4_3	1150	4	3	Air
1200_4_3	1200	4	3	Air
1150_8_3	1150	8	3	Air
1150_12_3	1150	12	3	Air
1200_4_5	1200	4	5	Air
1200_4_7	1200	4	7	Air
V1200_4_3	1200	4	3	Vacuum

2.2 Material characterization

The accuracy and the density of green bodies and sintered parts were evaluated by digital caliper measurements and weight values. The linear shrinkages in the X (recoater direction), Y (printhead direction), and Z (platform direction) axes were calculated by comparing the size of the actual components after curing and sintering. Pores and phases distribution were observed by scanning electron microscopy (SEM) equipped with energy dispersive x-ray spectroscopy (EDX) in a ZEISS Sigma 500 microscope and compared to x-ray diffraction (XRD) spectra detected in a Rigaku Smartlab SE with a Cu-Kα source, a step size of 0.02° and a scanning speed of 1° min^{-1}. XRD analyses were conducted on samples sintered at different temperatures/atmospheres with a heating rate of 3 °C min^{-1} for 4 hours.

The mechanical properties of sintered parts were evaluated by Vickers microhardness (HV) tested at 100 gf and a load time of 15 seconds and by 3-point bending testing (ASTM C1161-18) to assess the flexural strength [15].

3. Results and Discussion

3.1 Printing and densification

The powder flowability was sufficient to allow a repeatable and consistent printing process. Both saturation levels tested proved to produce a moderate powder bed density, as observed already in literature for irregular micrometric powders: the resulting green densities were 35.5 ± 0.9% and 33.0 ± 0.5% for 70% and 90% of BS, respectively [16,17]. Thus, densification was studied on parts produced with the former BS level.

It can be observed in **Fig. 2A** that the sintering temperature is the most influential parameter, while dwelling times and heating rates are negligible. Indeed, it can be observed that the relative density grows from 36.9% to about 55% and 70% by increasing the temperature from 1100 °C to 1150 °C and 1200 °C, respectively. It should be noted that sample 1100_4_3 is only affected by degassing during debinding and necking during sintering leading to a preliminary consolidation of the component and a minimal reduction in size (see **Fig. 2B**). Sintering becomes effective at 1150 °C, as revealed by the growth of the linear shrinkages above 15%, especially along the vertical direction (Z) owing to the collapse of the binder-rich interlayer regions during debinding [18]. The drastic change in densification is likely due to the melting of the glassy phase, which normally occurs in the 1100-1200 °C range depending on the exact composition of the simulant powder [19,20]. Dwelling time and heating rate are negligible: prolonged sintering (12 h) increases density by ~3% compared to shorter time (4 h), while changing the cycle ramp is not effective at all on densification and does not affect the mechanical stability of the material [21]. The temperature-dependent change in densification can be qualitatively appreciated as well by the appearance of the components in **Fig. 3**.

Interestingly, sintering in a vacuum promotes further densification (+ ~5% of density) with respect to corresponding conditions in static air, which was observed before for Mare simulants [14,22].

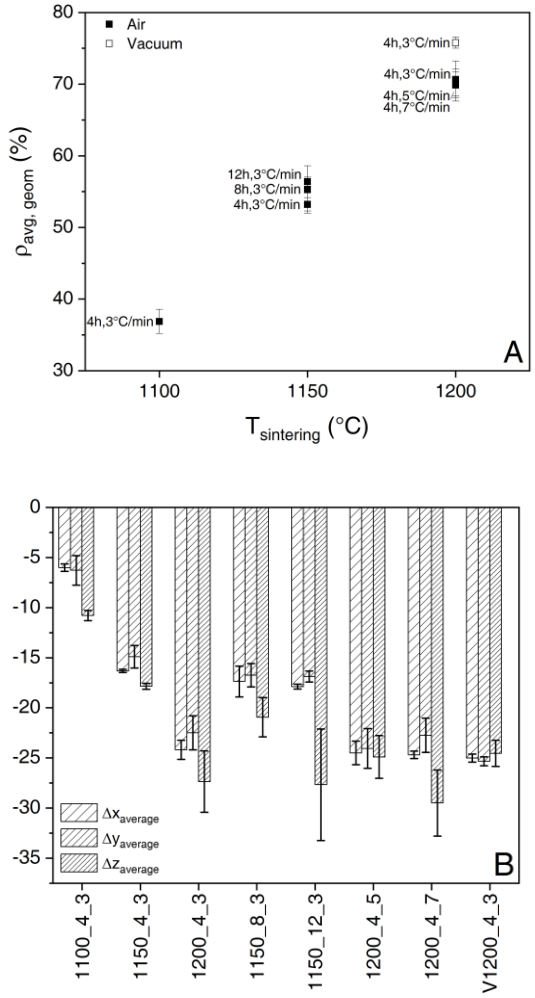

Fig. 2. A) Relative density values, and B) linear shrinkages along the X, Y, and Z axes of the sintered components

Copyright ©2024 by the International Astronautical Federation (IAF). All rights reserved.

Also, a colour change is observed, thus suggesting that phases development was different as well. The darker colour of LHS ceramics (see **Fig. 3**) sintered in a vacuum may result from the limited oxidation of iron and magnesium, and the reduction of Fe-rich basalt grains by residual carbon, coming from the decomposed organics in the PEG binder which was not completely pyrolyzed in an oxygen-free atmosphere [14,23].

In all cases, full densification was not achieved due to the low initial density of the green bodies which minimizes the contact points among particles and hinders the efficiency of volume-diffusive mechanisms during sintering.

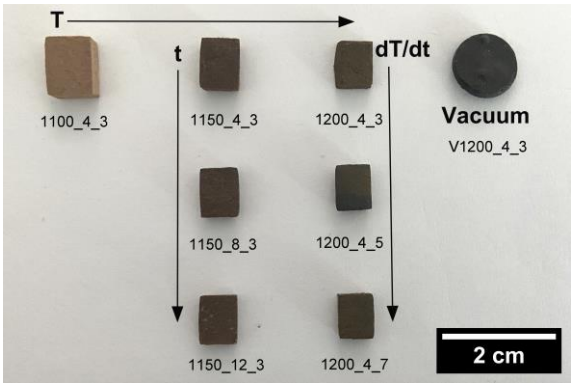

Fig. 3 Samples sintered in air (left) and in vacuum (right) at different sintering temperatures (T), times (t) and heating rates (dT/dt)

3.2 Microstructural development

The microstructural analysis reveals a widely spread residual porosity in all specimens, as expected from the low densification rates. The SEM images in **Fig. 4** show a progressive transition from a completely interconnected open porosity in samples featuring a density lower than 60% to a mixed porosity with closed spherical voids embedded in the ceramic matrix for samples sintered at 1150 °C or above.

In the case of parts sintered at 1100 °C (see **Fig. 4A**), particles have undergone just necking and their original morphologies can still be observed: these components need extreme care during handling because the mechanical resistance provided by solid necks among particles is minimal. It can be assumed that the linear shrinkages (see **Fig. 2B**) are mostly correlated to the removal of the polymeric binder, which is suggested by the discrepancy among Δz and $\Delta x/\Delta y$ as well: the collapse of the ligand-rich interlayer region after debinding is constant along the vertical axis, while volume-diffusive mechanisms at 1100 °C are negligible so densification in the intralayer regions is minimal.

At 1200 °C, individual particles cannot be detected, thus they are subject to a complete loss of their initial shape. Nearly spherical voids are present in the entirety of the components and their radius goes from a few microns to about 40 μm, as shown in **Fig. 4B**.

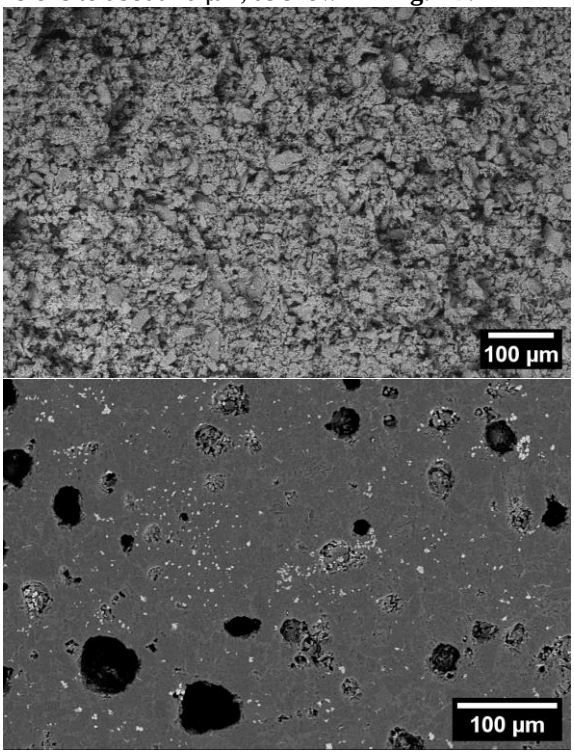

Fig. 4. Micrographies of A) a fracture surface of a 1100_4_3 specimen and B) a polished surface of a 1200_4_3 specimen

In **Fig. 5** EDX analyses of all samples display an Al/Ca/Na/Si-rich matrix of bytownite, which is a calcium-rich plagioclase feldspar of the type $(Ca_{1-x}Na_x)(Al(Al_ySi_{1-y})Si_2O_8)$ typical of Highlands soil. Secondary phases/inclusions are revealed by variations in the brightness of a few spots in the backscattered electrons signal in SEM micrographs: lighter areas correspond to localized increases in heavier elements such as iron and titanium. Nonetheless, segregations of magnesium and potassium can be observed as well.

XRD spectra in **Fig. 6A** confirm the presence of bytownite (COD ID: 9011200 - $Ca_{0.86}Na_{0.14}Al_{1.84}Si_{2.16}O_8$) as the main phase, while minor secondary peaks corresponding to ilmenite (COD ID: 9007011 - $Fe_{1.35}Ti_{0.65}O_3$), pyroxene (COD ID: 9001215 - $Fe_{0.084}Mg_{0.916}SiO_3$) and diopside (COD ID: 9005559 - $Al_{0.301}Ca_{0.752}K_{0.23}Mg_{0.749}Si_{1.968}O_6$), which is a clinopyroxene, were revealed at 2θ values not overlapping with bytownite. By comparing the theoretical compositions identified through XRD (**Fig. 6A**) with the elemental concentrations measured via EDX (**Fig. 6B**), it is possible to distinguish the matrix phase and confirm its chemical compositions: indeed, by averaging the signals from 1150_4_3B/C/D spots, it is obtained a bytownite with $x = 0.14$ and $y = 0.49$. The alkalis ratio x corresponds to the theoretical phase

Copyright ©2024 by the International Astronautical Federation (IAF). All rights reserved.

employed in the XRD, while *y* is larger. Nevertheless, the silicon signal might be increased by the contribution of the pyroxene-type inclusions.

The micrograph of the 1200_4_3 sample in **Fig. 5** highlights the redistribution of the diopside phase at the boundaries of the bytownite grains: the former undergoes melting below the sintering temperature, thus promoting supersolidus liquid phase sintering and densification of the components by pore filling effect.

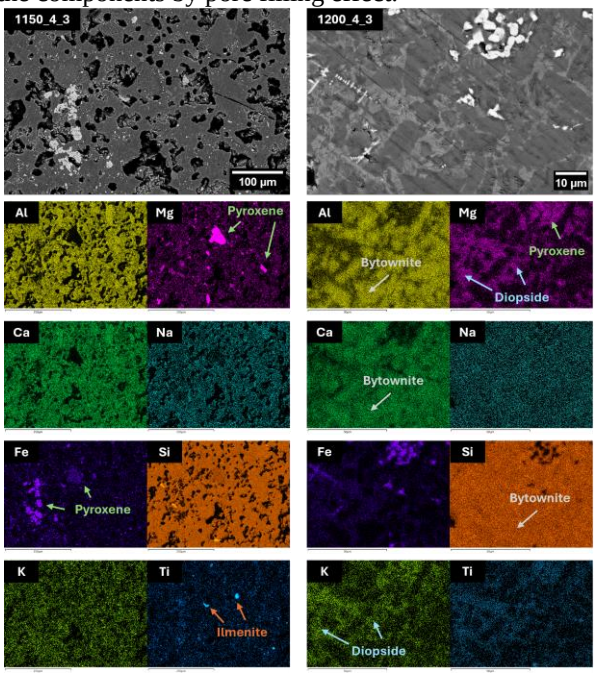

Fig. 5. SEM and EDX analyses of samples sintered in air at 1150 °C (left) and 1200 °C (right)

It can be observed that Fe-containing phases (ilmenite and pyroxene) associated XRD peaks decrease at higher sintering temperatures. Nevertheless, their presence cannot be excluded as already observed in the micrography of the 1200_4_3 specimen in **Fig. 5** and by the reported atomic concentrations of iron, magnesium, and titanium in specific sites (see **Fig. 6B**) corresponding to EDX analyses of inclusions shown in Appendix (**Fig. A1**). The 1200_4_3A spot shows a dendritic growth in the microstructure, characterized by an extremely high Fe content that should correspond to the nucleation of pure iron oxide grains, either hematite (Fe_2O_3) or magnetite (Fe_3O_4). Indeed, spectra of air-sintered samples above 1150 °C reveal also the appearance of magnetite, whose visible peak is indicated by the black arrow in **Fig. 6A**; hematite could be present as well, but its peaks overlap with those of ilmenite and bytownite, and they cannot be distinguished. Most likely, the high temperature, combined with the high diffusivity in presence of the liquid phase (i.e. molten diopside), facilitates the segregation of hematite from ilmenite which is in part reduced to magnetite.

Instead, the change in processing atmosphere is correlated to a reduction of the peaks intensity of both ilmenite and pyroxene, likely induced by the carbothermic reduction of iron-based oxides in a low pressure oxygen-poor atmosphere. Magnetite-associated peaks are absent as well, as the processing conditions are detrimental to its formation. Such change justifies the visible variation in colour (**Fig. 3**) of these samples with respect to the air-sintered counterparts, from a brownish appearance typical of iron oxides to darker grey. However, the presence of these oxidic inclusions was still detected within the diopside phase by EDX maps in the V1200_4_3 as well (**Fig. 7**), thus the reduction reaction process was not completed. Still, a drastic enrichment in iron was observed in spots V1200_4_3B/E, suggesting the progression toward metallic iron formation. The bytownite grains maintain an elemental balance similar to that observed in air-sintered components: the EDX analysis on the V1200_4_3 reveals $x = 0.20$ and $y = 0.46$ ratios.

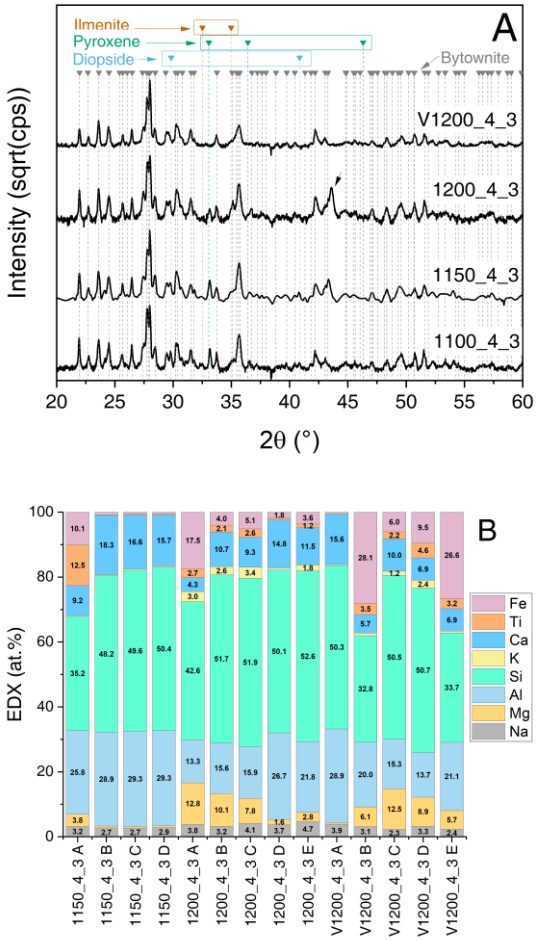

Fig. 6. A) XRD spectra and B) chemical compositions (at.%) measured by EDX of spots (shown in **Fig. A1**) of samples sintered in air at 1100 °C, 1150 °C and 1200 °C and in vacuum at 1200 °C

Copyright ©2024 by the International Astronautical Federation (IAF). All rights reserved.

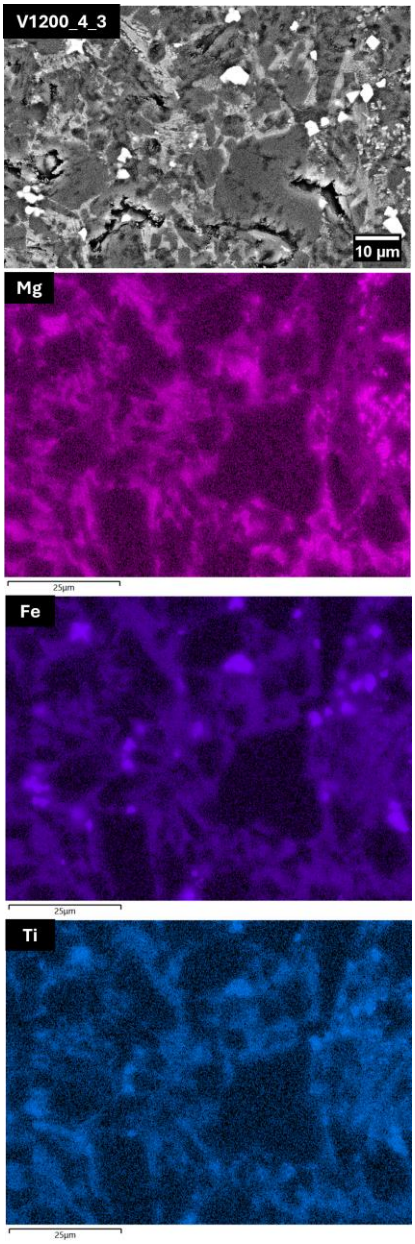

Fig. 7. SEM and EDX analysis of a sample sintered in vacuum at 1200 °C

3.3 Mechanical properties

The mechanical properties of the printed components were assessed for the parts sintered in air at 1200 °C. The microhardness was measured on the densified intralayer regions of each component and revealed statistically comparable results, as shown in **Fig. 8**. It should be noted that the measurements were performed on the denser areas to avoid the formation of irregular or deformed indentations owing to the collapse of pores in the sub-surface regions, nevertheless significant distinctions among the considered samples should not be expected even in case of macroscopic indentations because the residual porosity fraction and distribution is similar.

The printed specimens 1200_4_3 were analysed to determine their flexural strength by 3-point bending testing as well. The sintered components revealed a remarkable resistance of 66.95 ± 2.59 MPa. The standard deviation is limited, thus underlying the excellent repeatability of the printed parts performance which did not suffer from potential internal defects provoked by the printing process.

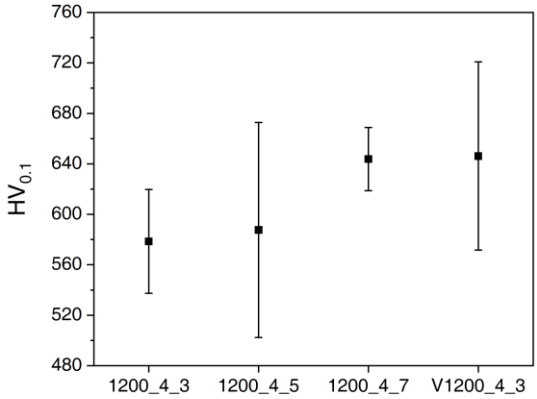

Fig. 8. Vickers microhardness values of the samples sintered in air at 1200 °C

5. Conclusions

The present study has shed a light on the influence of sintering parameters on the physical properties of BJT-printed highland lunar regolith ceramic parts.

It was determined that sintering temperature strongly influences the final density of the sintered components. The relative density grows from 36.9% to about 55% and 70% by increasing the temperature from 1100 °C to 1150 °C and 1200 °C, respectively. So, a 100 °C increase in heat-treatment temperature resulted in a 33% increase of relative density.

On the other hand, even a significant increase in dwelling time did not lead to a considerable raise in density. When switching from 4 h to 12 h dwelling times at 1200 °C, only a 4% increase in density was observed.

In addition, sintering the BJT-printed parts in a low vacuum led to a further + ~5% increase in the final parts' density. The future planned research activities would need to study this effect in additional details to simplify the adoption of BJT on the Moon.

Manufactured ceramic samples demonstrated excellent mechanical properties, yielding up to 640 $HV_{0.1}$ microhardness and ultimate flexural strength of 66.95 ± 2.59 MPa.

In summary, this study contributes significantly to the field of materials engineering and in-situ resource utilization by advancing the understanding of BJT-based AM of lunar regolith ceramic parts. The obtained results significantly broaden the possible fields of application of BJT for the long-term lunar exploration.

Copyright ©2024 by the International Astronautical Federation (IAF). All rights reserved.

Appendix

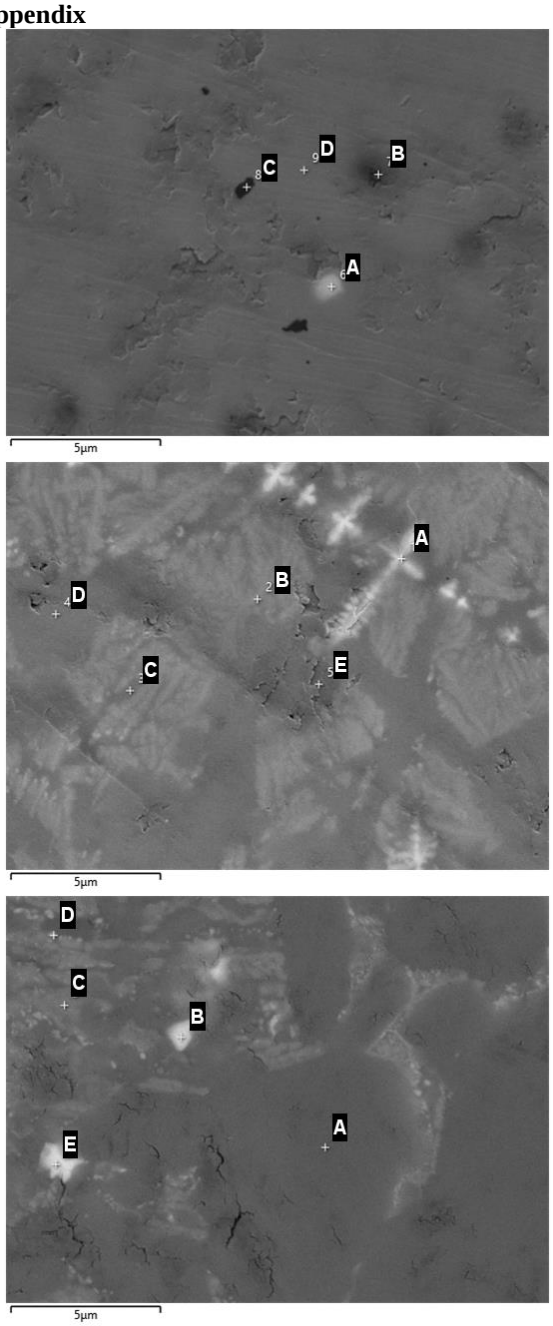

Fig. A1. EDX analyses sites for samples (top to bottom) 1150_4_3, 1200_4_3 and V1200_4_3

References

[1] Y. Wang, L. Hao, Y. Li, Q. Sun, M. Sun, Y. Huang, Z. Li, D. Tang, Y. Wang, L. Xiao, In-situ utilization of regolith resource and future exploration of additive manufacturing for lunar/martian habitats: A review, Appl. Clay Sci. 229 (2022) 106673. https://doi.org/10.1016/j.clay.2022.106673.

[2] S. Ulubeyli, Lunar shelter construction issues: The state-of-the-art towards 3D printing technologies, Acta Astronaut. 195 (2022) 318–343. https://doi.org/10.1016/j.actaastro.2022.03.033.

[3] M. Isachenkov, S. Chugunov, I. Akhatov, I. Shishkovsky, Regolith-based additive manufacturing for sustainable development of lunar infrastructure – An overview, Acta Astronaut. 180 (2021) 650–678. https://doi.org/10.1016/j.actaastro.2021.01.005.

[4] R. Wang, G. Qiao, G. Song, Additive manufacturing by laser powder bed fusion and thermal post-treatment of the lunar-regolith-based glass-ceramics for in-situ resource utilization, Constr. Build. Mater. 392 (2023) 132051. https://doi.org/10.1016/j.conbuildmat.2023.132051.

[5] M. Fateri, A. Meurisse, M. Sperl, D. Urbina, H.K. Madakashira, S. Govindaraj, J. Gancet, B. Imhof, W. Hoheneder, R. Waclavicek, C. Preisinger, E. Podreka, M.P. Mohamed, P. Weiss, Solar Sintering for Lunar Additive Manufacturing, J. Aerosp. Eng. 32 (2019). https://doi.org/10.1061/(ASCE)AS.1943-5525.0001093.

[6] L.A. Taylor, T.T. Meek, Microwave Sintering of Lunar Soil: Properties, Theory, and Practice, J. Aerosp. Eng. 18 (2005) 188–196. https://doi.org/10.1061/(ASCE)0893-1321(2005)18:3(188).

[7] B. Khoshnevis, J. Zhang, Extraterrestrial construction using contour crafting, in: University of Texas at Austin (Ed.), 2012 Int. Solid Free. Fabr. Symp., 2012. https://doi.org/http://dx.doi.org/10.26153/tsw/15347.

[8] C. Xiao, K. Zheng, S. Chen, N. Li, X. Shang, F. Wang, J. Liang, S.B. Khan, Y. Shen, B. Lu, H. Ma, Z. Chen, Additive manufacturing of high solid content lunar regolith simulant paste based on vat photopolymerization and the effect of water addition on paste retention properties, Addit. Manuf. 71 (2023) 103607. https://doi.org/10.1016/j.addma.2023.103607.

[9] M. Isachenkov, A.M. Grande, G. Sala, Optimizing lunar regolith for vat polymerization and sintering: pre-processing & mineral composition impact, Ceram. Int. 50 (2024) 32265–32277. https://doi.org/10.1016/j.ceramint.2024.06.034.

[10] S.L. Taylor, A.E. Jakus, K.D. Koube, A.J. Ibeh, N.R. Geisendorfer, R.N. Shah, D.C. Dunand, Sintering of micro-trusses created by extrusion-3D-printing of lunar regolith inks, Acta Astronaut. 143 (2018) 1–8. https://doi.org/10.1016/j.actaastro.2017.11.005.

Copyright ©2024 by the International Astronautical Federation (IAF). All rights reserved.

[11] G. Cesaretti, E. Dini, X. De Kestelier, V. Colla, L. Pambaguian, Building components for an outpost on the Lunar soil by means of a novel 3D printing technology, Acta Astronaut. 93 (2014) 430–450. https://doi.org/10.1016/j.actaastro.2013.07.034.

[12] A. Zocca, J. Lüchtenborg, T. Mühler, J. Wilbig, G. Mohr, T. Villatte, F. Léonard, G. Nolze, M. Sparenberg, J. Melcher, K. Hilgenberg, J. Günster, Enabling the 3D Printing of Metal Components in μ-Gravity, Adv. Mater. Technol. 4 (2019) 1900506. https://doi.org/10.1002/admt.201900506.

[13] M. Isachenkov, S. Chugunov, Z. Landsman, I. Akhatov, A. Metke, A. Tikhonov, I. Shishkovsky, Characterization of novel lunar highland and mare simulants for ISRU research applications, Icarus. 376 (2022) 114873. https://doi.org/10.1016/j.icarus.2021.114873.

[14] A. Meurisse, J.C. Beltzung, M. Kolbe, A. Cowley, M. Sperl, Influence of Mineral Composition on Sintering Lunar Regolith, J. Aerosp. Eng. 30 (2017). https://doi.org/10.1061/(ASCE)AS.1943-5525.0000721.

[15] M. Mariani, R. Beltrami, P. Brusa, C. Galassi, R. Ardito, N. Lecis, 3D printing of fine alumina powders by binder jetting, J. Eur. Ceram. Soc. 41 (2021) 5307–5315. https://doi.org/10.1016/j.jeurceramsoc.2021.04.006.

[16] F. Bertolini, M. Mariani, E. Mercadelli, C. Baldisserri, C. Galassi, C. Capiani, R. Ardito, N. Lecis, 3D printing of potassium sodium niobate by binder jetting: Printing parameters optimisation and correlation to final porosity, J. Mater. Res. Technol. 29 (2024) 4597–4606. https://doi.org/10.1016/j.jmrt.2024.02.145.

[17] M. Mariani, E. Mercadelli, L. Cangini, C. Baldisserri, C. Galassi, C. Capiani, N. Lecis, Additive Manufacturing of Piezoelectric Niobium-Doped Lead Zirconate Titanate (PZT-N) by Binder Jetting, Crystals. 13 (2023) 883. https://doi.org/10.3390/cryst13060883.

[18] P. Warren, N. Raju, H. Ebrahimi, M. Krsmanovic, S. Raghavan, J. Kapat, R. Ghosh, Effect of sintering temperature on microstructure and mechanical properties of molded Martian and Lunar regolith, Ceram. Int. 48 (2022) 35825–35833. https://doi.org/10.1016/j.ceramint.2022.07.329.

[19] K.W. Farries, P. Visintin, S.T. Smith, P. van Eyk, Sintered or melted regolith for lunar construction: state-of-the-art review and future research directions, Constr. Build. Mater. 296 (2021) 123627. https://doi.org/10.1016/j.conbuildmat.2021.123627.

[20] A. Zocca, M. Fateri, D. Al-Sabbagh, J. Günster, Investigation of the sintering and melting of JSC-2A lunar regolith simulant, Ceram. Int. 46 (2020) 14097–14104. https://doi.org/10.1016/j.ceramint.2020.02.212.

[21] T. HOSHINO, S. WAKABAYASHI, S. YOSHIHARA, N. HATANAKA, Key Technology Development for Future Lunar Utilization— Block Production Using Lunar Regolith, Trans. JAPAN Soc. Aeronaut. Sp. Sci. Aerosp. Technol. JAPAN. 14 (2016) Pk_35-Pk_40. https://doi.org/10.2322/tastj.14.Pk_35.

[22] M. Fateri, R. Sottong, M. Kolbe, J. Gamer, M. Sperl, A. Cowley, Thermal properties of processed lunar regolith simulant, Int. J. Appl. Ceram. Technol. 16 (2019) 2419–2428. https://doi.org/10.1111/ijac.13267.

[23] N. Lecis, M. Mariani, R. Beltrami, L. Emanuelli, R. Casati, M. Vedani, A. Molinari, Effects of process parameters, debinding and sintering on the microstructure of 316L stainless steel produced by binder jetting, Mater. Sci. Eng. A. 828 (2021) 142108. https://doi.org/10.1016/j.msea.2021.142108.